AIP Journal of Applied Physics

Empirically based device modeling of bulk heterojunction organic photovoltaics

Adrien Pierre, Shaofeng Lu, Ian A. Howard, Antonio Facchetti, and Ana Claudia Arias

Citation: Journal of Applied Physics **113**, 154506 (2013); doi: 10.1063/1.4801662
View online: http://dx.doi.org/10.1063/1.4801662
View Table of Contents: http://scitation.aip.org/content/aip/journal/jap/113/15?ver=pdfcov
Published by the AIP Publishing

Empirically based device modeling of bulk heterojunction organic photovoltaics

Adrien Pierre,[1] Shaofeng Lu,[2] Ian A. Howard,[3] Antonio Facchetti,[2] and Ana Claudia Arias[1,a)]

[1]*Department of Electrical Engineering and Computer Sciences, University of California, Berkeley, California 94720, USA*
[2]*Polyera Corporation, 8045 Lamon Avenue, Skokie, Illinois 60077, USA*
[3]*Max Planck Institute for Polymer Research, Ackermannweg 10, 55128 Mainz, Germany*

(Received 14 January 2013; accepted 25 March 2013; published online 19 April 2013)

We develop an empirically based optoelectronic model to accurately simulate the photocurrent in organic photovoltaic (OPV) devices with novel materials including bulk heterojunction OPV devices based on a new low band gap dithienothiophene-DPP donor polymer, P(TBT-DPP), blended with $PC_{70}BM$ at various donor-acceptor weight ratios and solvent compositions. Our devices exhibit power conversion efficiencies ranging from 1.8% to 4.7% at AM 1.5G. Electron and hole mobilities are determined using space-charge limited current measurements. Bimolecular recombination coefficients are both analytically calculated using slowest-carrier limited Langevin recombination and measured using an electro-optical pump-probe technique. Exciton quenching efficiencies in the donor and acceptor domains are determined from photoluminescence spectroscopy. In addition, dielectric and optical constants are experimentally determined. The photocurrent and its bias-dependence that we simulate using the optoelectronic model we develop, which takes into account these physically measured parameters, shows less than 7% error with respect to the experimental photocurrent (when both experimentally and semi-analytically determined recombination coefficient is used). Free carrier generation and recombination rates of the photocurrent are modeled as a function of the position in the active layer at various applied biases. These results show that while free carrier generation is maximized in the center of the device, free carrier recombination is most dominant near the electrodes even in high performance devices. Such knowledge of carrier activity is essential for the optimization of the active layer by enhancing light trapping and minimizing recombination. Our simulation program is intended to be freely distributed for use in laboratories fabricating OPV devices. © *2013 AIP Publishing LLC*.
[http://dx.doi.org/10.1063/1.4801662]

INTRODUCTION

Materials development in the field of bulk heterojunction (BHJ) organic photovoltaics (OPV) has driven device power conversion efficiencies (PCEs) of tandem solar cells to 10.7% (Ref. 1) and of solution processed single junction solar cells to >9.1%.[2] Fundamental understanding of the physical processes inside BHJ OPVs has also significantly progressed.[3–6] Semiconductor device modeling can enable insightful interpretation of experimental results to enable rapid PCE optimization, provided that the model encompasses the correct fundamental processes. Most semiconductor modeling programs available today are designed to simulate conventional inorganic devices, with only a few having amendments to simulate organic semiconductors.[7] However, there is a clear understanding that more thorough physical models are necessary for useful simulation of BHJ OPV behavior.[8–14] A simple, broadly applicable BHJ OPV model is clearly desirable considering the large number of laboratories fabricating these devices with new organic semiconductor, interlayer, and electrode materials.

In this work, we develop upon previous BHJ OPV models in order to develop an empirically based model taking into account recent advances in the understanding of charge generation and recombination mechanisms. A novel polymer donor–small molecule acceptor BHJ blend, poly[{2,6-(4,8-didodecylbenzo[1,2-b:4,5-b′]dithiophene)}-*alt*-{5,5-(2,5-bis(2-butyloctyl)-3,6-dithiophen-2-yl-2,5-dihydropyrrolo[3,4-c]pyrrole-1,4-dione)}] (P(TBT-DPP)): [6,6]-phenylC_{71} butyric acid methyl ester ($PC_{70}BM$), is characterized, and the results are used to validate the model presented here. P(TBT-DPP) is a π-conjugated donor polymer exhibiting high molecular weight ($Mn = 27$ kDa, $PDI = 6.5$ vs. PS standard), low optical band gap (1.5 eV), excellent operational air stability, and high PCE of 4.7% when mixed with $PC_{70}BM$ acceptors without thermal treatment. Mobility, bimolecular recombination coefficient, exciton quenching, permittivity, and optical constants for many different devices are experimentally determined using several techniques. The trends observed across various BHJ films serve to gain insights into the underlying factors governing the device behavior. These parameters are input into the model. Using the optical constants of all the device layers and exciton quenching in the active layer, the model determines the spatial distribution of charge generation rate under steady illumination. Subsequently,

a)Author to whom correspondence should be addressed. Electronic mail: acarias@eecs.berkeley.edu.

the generation rates, mobility, bimolecular recombination coefficients, and permittivity are input into the current continuity equations to compute photocurrent and carrier concentration. The agreement of the simulated and measured carrier concentrations and photocurrent–voltage characteristics for a variety of devices without the use of fitted parameters is a strong indicator of the physical completeness and accuracy of our model. This accuracy allows significant conclusions regarding the efficiency limitations caused by carrier generation and non-geminate recombination (bimolecular free carrier recombination) rates inside the device as a function of bias. Such detailed understanding is not only useful for post *hoc* device analysis but also enables predictive theoretical device optimization. These results from the model can serve to optimize the compositional grading of future devices in order to maximize light trapping and free carrier generation while minimizing non-geminate recombination.

EXPERIMENTS AND METHODS

Synthetic details

Figure 1 illustrates the synthesis of P(TBT-DPP). 2,6-Di (trimethylstannyl)-4,8-didodecylbenzo[1,2-b:4,5-b′]dithiophene (29.8 mg, 35 μmol), 3,6-bis-(5-bromothiophen-2-yl)-2,5-Bis-(2-butyloctyl)-pyrrolo[3,4-c]pyrrole-1,4-dione (27.8 mg, 35 μmol), $Pd_2(dba)_3$ (1.3 mg, 4 mol. %), and tri(*o*-tolyl)phosphine (1.7 mg, 16 mol. %) were mixed in anhydrous chlorobenzene (5 ml) under argon and stirred at 133 °C for 72 h in a 100 ml storage vessel. After cooling down, it was poured into MeOH (50 ml), filtered, and dried under vacuum oven to give a black solid (38.6 mg, yield 95%). The crude was soxhlet extracted with ethyl acetate, 1,4-dioxane, and chloroform, successively. The chloroform extract was poured into MeOH (100 ml), and the solid was collected. Finally, a maroon solid (32.1 mg, yield 79%, $Mn = 27$ kDa, $PDI = 6.5$) was obtained. The elemental analysis is as follows: Calcd. C 74.56, H 9.21, N 2.42; Found: C 74.68, H, 8.97, N 2.49.

BHJ OPV device fabrication and characterization

Devices are fabricated on 15 Ω/square indium tin oxide (ITO) on glass substrates that are cleaned by 10 min of ultrasonication in acetone and then in isopropanol. The cleaned substrates are treated under UV ozone for 30 min, immediately followed by spin coating 35 nm of Clevios™ P VP AI 4083 poly(3,4-ethylenedioxythiophene)-poly(styrenesulfonate) (PEDOT:PSS) as the hole injection layer. The PEDOT:PSS is subsequently annealed at 130 °C in air for 10 min to remove moisture from the deposited film. P(TBT-DPP), the donor, and $PC_{70}BM$, the acceptor, are weighed in air, but solutions of these materials are prepared inside a nitrogen glovebox using anhydrous solvents. P(TBT-DPP) and $PC_{70}BM$ are separately mixed in 19:1 and 9:1 chloroform ($CHCl_3$):1,2 Dichlorobenzene (DCB) to a concentration of 15 mg/ml to yield high and low performing devices, respectively. The solutions are heated overnight at 40 °C to ensure full dissolution, especially considering the high molecular weight of P(TBT-DPP). The desired P(TBT-DPP):$PC_{70}BM$ compositions are mixed before spin casting after the initial solutions have been cooled down. 1:1, 3:7, and 1:5 P(TBT-DPP):$PC_{70}BM$ by weight compositions are prepared in 19:1 $CHCl_3$:DCB while 1:1, 1:2, and 1:5 P(TBT-DPP):$PC_{70}BM$ compositions are prepared in 9:1 $CHCl_3$:DCB. The active layers are spun at 2000 rpm in a nitrogen glovebox to yield film thicknesses of 135 nm ± 5 nm measured using a Dektak profilometer. The cathode is formed by thermally evaporating 7 Å of LiF, followed by 100 nm of Al at 3×10^{-6} Torr inside the same glovebox to yield an active area of 3.9 mm^2. Devices are tested in air using a calibrated Thermal-Oriel 300W solar simulator under AM 1.5G at 100 mW/cm^2 solar illumination. Experimental photocurrents are determined by subtracting the dark current from the illuminated current.

Electrical and optical measurements

Electron and hole mobilities are extracted from space-charge limited current (SCLC) measurements using electron and hole only devices, respectively. The layer stack of hole only devices is glass/ITO/PEDOT:PSS/P(TBT-DPP):$PC_{70}BM$ BHJ/Au while that of electron only devices is glass/ITO/TiO_2/P(TBT-DPP):$PC_{70}BM$ BHJ/LiF/Al. Current density–voltage (J–V) characteristics are measured using a Keithley 236 source-measurement unit. Bimolecular recombination coefficients and carrier concentrations are experimentally determined using a double-pulsed laser method[4] while the device is forward biased in the power generation region, from 0 to 0.6 V. Two lasers of 532 nm wavelength are used to excite the sample at the same intensity as AM 1.5 light (100 mW/cm^2) since the recombination coefficients are intensity-dependent.[3] The optical constants of P(TBT-DPP) and $PC_{70}BM$ are determined by a combination of ellipsometry and photospectrometry, while those of PEDOT:PSS and Al are taken from an optical matrix program written by Burkhard *et al.*[11] (see supplementary material for optical constants[34]). The dielectric constant of P(TBT-DPP) and $PC_{70}BM$ are determined to be 1.9 and 3.02, respectively, by measuring the low frequency (1 kHz) response fabricating glass/ITO/P(TBT-DPP):$PC_{70}BM$ BHJ/Al devices using an Agilent B1500A semiconductor device analyzer.

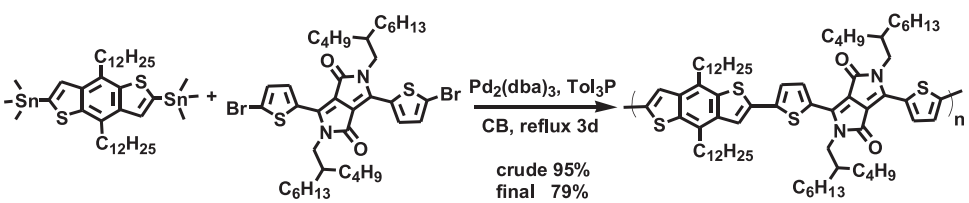

FIG. 1. Synthesis of Poly[{2,6-(4,8-didodecylbenzo[1,2-b:4,5-b′]dithiophene)}-*alt*-{5,5-(2,5-bis(2-butyloctyl)-3,6-dithiophen-2-yl-2,5-dihydropyrrolo[3,4-c] pyrrole-1,4-dione)}] (P(TBT-DPP)).

Exciton quenching efficiency for P(TBT-DPP):$PC_{70}BM$ BHJs is determined through photoluminescence (PL) spectroscopy using a Horiba NanoLog Spectrofluorometer equipped with a liquid nitrogen cooled InGaAs photodetector. Two excitation wavelengths are selected that absorb mutually exclusively in P(TBT-DPP) (650 nm) and $PC_{70}BM$ (475 nm). The expected normalized PL spectrum for a BHJ if no exciton quenching was to occur, $PL_{0,norm}$, is first computed according to Eqs. (1) and (2) for 475 nm and 650 nm excitation, respectively. f_A is the acceptor composition fraction of the BHJ film under investigation, $PL(\lambda)$ and OD are the PL emission spectrum and optical density for either pristine P(TBT-DPP) (subscript D) or $PC_{70}BM$ (subscript A) baselines excited at 475 nm or 650 nm. Normalizing the PL spectrum with respect to optical density removes dependence on film thickness

$$PL_{0,norm,475\mathrm{nm}}(\lambda) = f_A \cdot \frac{PL_{A,475\mathrm{nm}}(\lambda)}{1-10^{-OD_A(475\mathrm{nm})}} + [1-f_A] \cdot \frac{PL_{D,475\mathrm{nm}}(\lambda)}{1-10^{-OD_D(475\mathrm{nm})}}, \quad (1)$$

$$PL_{0,norm,650\mathrm{nm}}(\lambda) = f_A \cdot \frac{PL_{A,650\mathrm{nm}}(\lambda)}{1-10^{-OD_A(650\mathrm{nm})}} + [1-f_A] \cdot \frac{PL_{D,650\mathrm{nm}}(\lambda)}{1-10^{-OD_D(650\mathrm{nm})}}. \quad (2)$$

The PL emission spectrum for the BHJ is also normalized to its own optical density at both excitation wavelengths as shown in Eqs. (3) and (4)

$$PL_{BHJ,norm,475\mathrm{nm}}(\lambda) = \frac{PL_{BHJ}(475\mathrm{nm})}{1-10^{-OD_{BHJ}(475\mathrm{nm})}}, \quad (3)$$

$$PL_{BHJ,norm,650\mathrm{nm}}(\lambda) = \frac{PL_{BHJ}(650\mathrm{nm})}{1-10^{-OD_{BHJ}(650\mathrm{nm})}}. \quad (4)$$

The normalized difference between the expected PL spectrum without quenching (Eqs. (1) and (2)) and PL spectrum of the BHJ (Eqs. (3) and (4)) is integrated over the whole spectrum to yield exciton quenching efficiency as shown in Eqs. (5) and (6) for $PC_{70}BM$ and P(TBT-DPP), respectively.

$$\eta_A = \int \frac{\left(PL_{0,norm,475\mathrm{nm}}(\lambda) - PL_{BHJ,norm,475\mathrm{nm}}(\lambda)\right)}{PL_{0,norm,475\mathrm{nm}}(\lambda)} d\lambda, \quad (5)$$

$$\eta_D = \int \frac{\left(PL_{0,norm,650\mathrm{nm}}(\lambda) - PL_{BHJ,norm,650\mathrm{nm}}(\lambda)\right)}{PL_{0,norm,650\mathrm{nm}}(\lambda)} d\lambda. \quad (6)$$

The experimentally determined input parameters to the device model are the mobility, bimolecular recombination coefficient, exciton quenching, permittivity, optical constants, device layer stack, and active layer morphology as a function of position between anode and cathode (known as depth). P(TBT-DPP):$PC_{70}BM$ BHJs are morphologically homogenous from anode to cathode as confirmed by TEM tomography (see supplementary material for TEM tomography images[34]) and are modeled as such.

Device simulations

The first step in the simulation is determining the depth-dependent generation profile (anode to cathode) in the device using an optical transfer matrix model developed by Burkhard *et al.*[11] that also takes into account parasitic absorption at the electrodes. Two modifications are made to the optical generation calculator: (1) separating the active layer into thin slices (1 nm) to allow modeling of depth-varying morphology and (2) using Eq. (7) to calculate free-carrier generation as a function of depth, $G(x)$, from the wavelength-dependent exciton quenching efficiency, $\eta_{ex}(x,\lambda)$, and computed exciton generation rate, $G_{ex}(x,\lambda)$. The exciton quenching efficiency, $\eta_{ex}(x,\lambda)$, depends on the fraction of light absorbed by the donor or acceptor phase and the associated exciton dissociation efficiency for each phase.

$$G(x) = \int_{all\ \lambda} G_{ex}(x,\lambda)\eta_{ex}(x,\lambda)d\lambda. \quad (7)$$

The second phase of the simulation computes the photocurrent and recombination depth profile. Equations (8) and (9) are the drift and diffusion photocurrent equations for electrons and holes, respectively.

$$J_{ph,n}(x) = q\mu_n(x)n(x)E(x) + qD_n(x)\frac{dn(x)}{dx}, \quad (8)$$

$$J_{ph,p}(x) = q\mu_p(x)p(x)E(x) - qD_p(x)\frac{dp(x)}{dx}, \quad (9)$$

q, k_B, T, x, and E are the elementary charge, Boltzmann constant, temperature, distance from the cathode, and electric field, respectively. The internal electric field, $E(x)$, varies spatially according to changes in electric permittivity. Space-charge effects in BHJs were not taken into account since they are not significant according to literature.[8] This assertion is in the end further supported by the accuracy of our model. n, p, μ_n, μ_p, D_n, and D_p are the electron and hole concentrations, mobilities, and diffusion coefficients, respectively. Both trap and charge density affect the Einstein relationship in disordered semiconductors.[5,15] However, for a low trap density organic semiconductor in conjunction with the non-degenerate carrier concentrations during operation ($\leq\sim 10^{22}\,\mathrm{m}^{-3}$), one can approximate that the classical Einstein relation, $\frac{D}{\mu} = \frac{k_B T}{q}$, holds as in Eqs. (8) and (9).[15] Equations (10) and (11) are the steady-state photocurrent continuity equations for electrons and holes, respectively, where G and R are the charge generation and recombination rates, respectively.

$$\frac{dJ_{ph,n}(x)}{dx} = -q(G(x) - R(x)), \quad (10)$$

$$\frac{dJ_{ph,p}(x)}{dx} = q(G(x) - R(x)). \quad (11)$$

The general form of non-geminate recombination is shown in Eq. (12) with bimolecular recombination coefficient $B(x)$ and intrinsic carrier concentration n_i. n_i is negligible compared to

the photogenerated carrier concentration as a result of the relatively high bandgaps of conjugated polymers.[16]

$$R(x) = B(x)(n(x)p(x) - n_i^2). \tag{12}$$

A 5th order Runge-Kutta algorithm (BVP5c in MATLAB) is implemented to solve the two coupled differential equations resulting from merging Eqs. (8) and (9) with Eqs. (10) and (11), respectively. The boundary conditions to this set of differential equations are the electron and hole concentrations at the electrodes. These boundary conditions are the only parameters of our model that we do not experimentally determine. Assuming ohmic contacts, the large energetic separation between the anode and LUMO and cathode and HOMO allow electron and hole concentrations to be approximated to zero at the anode and cathode interfaces, respectively. The absence of minority carriers at both electrodes is a boundary condition of infinite surface recombination velocity, which is typically used when modeling BHJ OPVs.[8,14,17] The boundary condition for 9:1 $CHCl_3$:DCB devices is taken to be the same as in previous models for low performance polymer-fullerene BHJs,[8,12] $\sim 10^{25}$ carriers/m^3. The boundary conditions for the 19:1 solvent devices are then determined by comparing the ratio of the 9:1 and 19:1 $CHCl_3$:DCB device dark currents under low reverse bias in order to neglect forward bias diffusion current, thus $J \propto n_o \mu$, where n_o is the carrier density near the surface. 19:1 $CHCl_3$:DCB devices have a boundary condition of 6.5×10^{23} carriers/m^3. The built-in potential in our devices is set to 1.1 eV, the work function difference between PEDOT:PSS, 5.2 eV, and Aluminum, 4.1 eV.

RESULTS

Figure 2 and Table I correspondingly show the J–V curves and solar cell characteristics for devices cast from 9:1 and 19:1 $CHCl_3$:DCB solvent ratios. Note that 19:1 $CHCl_3$:DCB devices yield superior performance compared to 9:1 $CHCl_3$:DCB devices. Optimal PCE is achieved at 3:7 and 1:2 P(TBT-DPP):$PC_{70}BM$ for 19:1 and 9:1 $CHCl_3$:DCB devices, respectively. The performance variation of these devices forms a wide basis to assess the breadth of the applicability of our model.

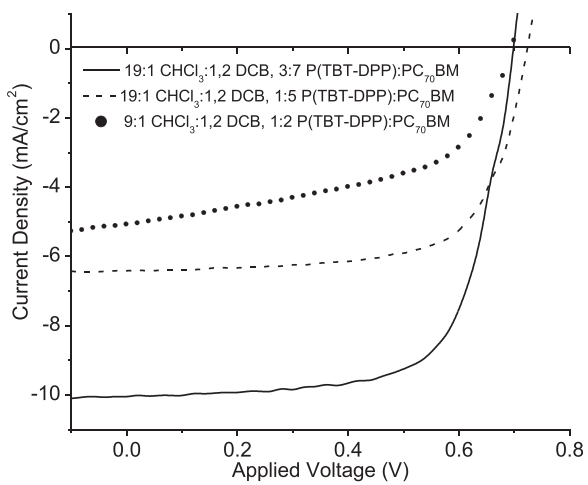

FIG. 2. Current density-voltage characteristics for 19:1 $CHCl_3$:DCB, 3:7P(TBT-DPP):$PC_{70}BM$ (solid line), 19:1 $CHCl_3$:DCB, 1:5P(TBT-DPP):$PC_{70}BM$ (dashed line), and 9:1 $CHCl_3$:DCB, 1:2P(TBT-DPP):$PC_{70}BM$ (dotted line) under AM 1.5G.

TABLE I. Short circuit current (J_{SC}), open circuit voltage (V_{OC}), fill factor (FF), and PCE for the devices of Figure 1 where D:A denotes the P(TBT-DPP):$PC_{70}BM$ weight ratio.

Sample	J_{SC} (mA/cm^2)	V_{OC} (V)	FF	PCE (%)
19:1 $CHCl_3$:DCB, 3:7 D:A	10.05	0.7	0.687	4.75
19:1 $CHCl_3$:DCB, 1:5 D:A	6.41	0.72	0.686	3.13
9:1 $CHCl_3$:DCB, 1:2 D:A	5.07	0.69	0.522	1.82

The charge mobility, charge generation, bimolecular recombination coefficient, permittivity, and optical constant parameters are related to the photoactive film morphology, which is highly dependent on the spin casting solvent and donor-acceptor composition.[18] All these parameters are characterized for cells fabricated from both 19:1 and 9:1 $CHCl_3$:DCB solvent ratios and for various P(TBT-DPP):$PC_{70}BM$ compositions. The retrieved information in itself imparts much information about the device characteristics but furthermore allows us to accurately simulate this broad range of performance with the previously introduced fit parameter-free model.

Electron and hole mobility is determined by fitting SCLC curves to the Mott-Gurney expression for trap-free SCLC according to Eq. (13)

$$J = \frac{9}{8}\varepsilon\mu\frac{V_a^2}{L^3}. \tag{13}$$

ε, μ, V_a, and L are the electric permittivity, charge carrier mobility (electron or hole), applied voltage, and active layer thickness, respectively. Figures 3(a) and 3(b) accordingly show the electron and hole SCLC curves and their fits with respect to Eq. (13) for the 19:1 $CHCl_3$:DCB devices with 1:1, 3:7, and 1:5 P(TBT-DPP):$PC_{70}BM$ composition ratios. 9:1 $CHCl_3$:DCB devices also generated close fits with respect to Eq. (13), which is indicative of a trap-free active layer for a variety of BHJ film formulations. Figure 4(a) shows the extracted mobility values for 9:1 and 19:1 $CHCl_3$:DCB devices for various P(TBT-DPP):$PC_{70}BM$ compositions. The hole mobility remains relatively invariant for 19:1 $CHCl_3$:DCB devices while that of the electron increases when the $PC_{70}BM$ weight ratio is increased. However the mobility for 9:1 $CHCl_3$:DCB devices is lower when compared to 19:1 $CHCl_3$:DCB devices, which is responsible for the low FF shown in Table I. The marked increase in hole mobility for the 9:1 $CHCl_3$:DCB devices with larger $PC_{70}BM$ compositions is believed to be the result of either the formation of $PC_{70}BM$ cations which serve as a hole transporters[19] or improved crystallinity of the polymer donor phase.[20]

Recombination is another important property of BHJs. An electron and hole in a BHJ recombine in their charge transfer (CT) state either geminately, if both carriers have never been dissociated, or non-geminately if both carriers had been dissociated into free carriers.[21] Geminate recombination is implicit in the exciton quenching efficiency, $\eta_{ex}(x)$. Non-geminate recombination in homogenous low-mobility

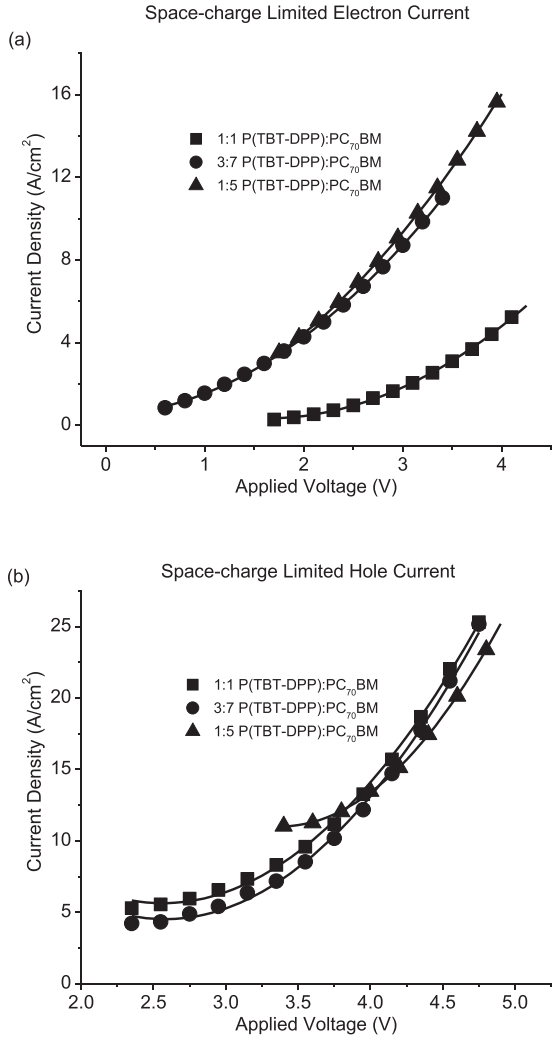

FIG. 3. Electron (a) and hole (b) SCLC and fits (solid lines) generated according to Eq. (13) for devices cast from 19:1 $CHCl_3$:DCB with 1:1, 3:7, and 1:5 P(TBT-DPP):$PC_{70}BM$ compositions.

semiconductors occurs in the diffusive-limited regime and is often modeled by Langevin recombination.[22]

$$B(x) = \frac{q}{\varepsilon(x)}\left(\mu_n(x) + \mu_p(x)\right). \tag{14}$$

However, slowest carrier-limited Langevin recombination is believed to be relevant in BHJs as a consequence of the segregation of electrons and holes into acceptor and donor domains, respectively.[23]

$$B(x) = \frac{q}{\varepsilon(x)}\left[\frac{\mu_n(x)\mu_p(x)}{\mu_n(x) + \mu_p(x)}\right]. \tag{15}$$

Figure 4(b) shows the bimolecular recombination coefficients for both 9:1 and 19:1 $CHCl_3$:DCB devices for various P(TBT-DPP):$PC_{70}BM$ compositions. These coefficients are experimentally measured and calculated from Eq. (15) using measured mobility and permittivity. Both 0.5 and 0.7 $PC_{70}BM$ weight compositions for the 19:1 $CHCl_3$:DCB devices exhibit close matches between slowest carrier Langevin

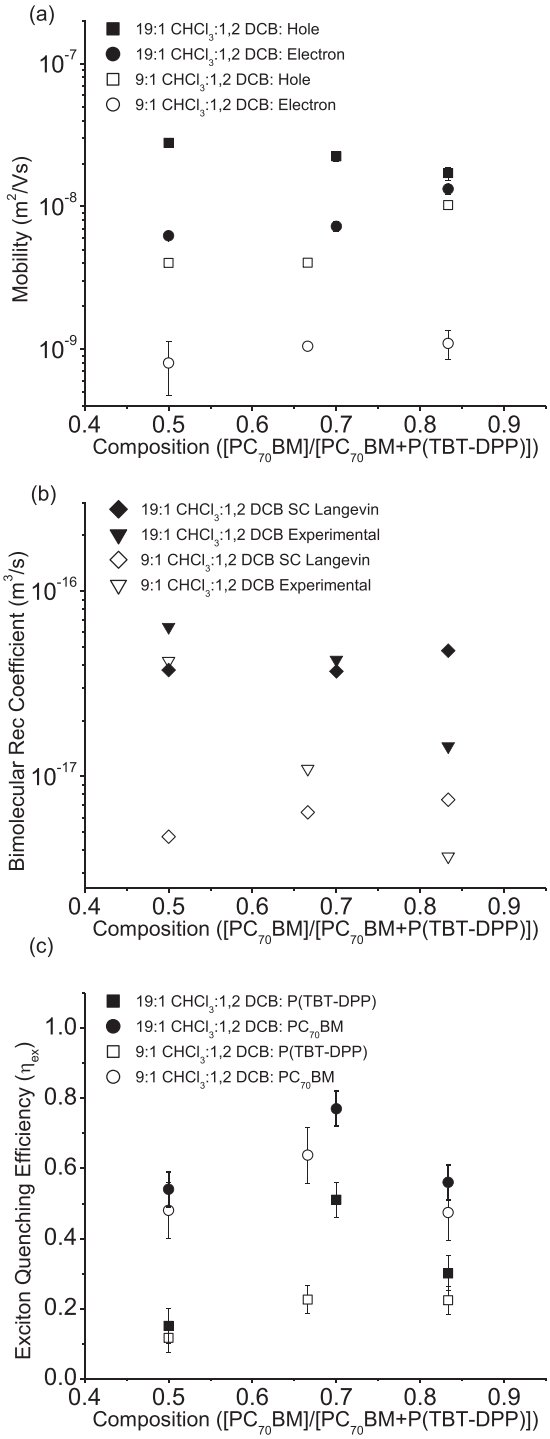

FIG. 4. Mobility determined through space-charge limited current (a), bimolecular recombination coefficients determined experimentally from electro-optical pump probing and analytically from slowest-carrier limited Langevin (SC Langevin) recombination using Eq. (15) (b) and exciton quenching efficiency determined through photoluminescence spectroscopy (c) for devices cast from 9:1 and 19:1 $CHCl_3$:DCB with various P(TBT-DPP):$PC_{70}BM$ weight compositions.

and experimentally determined recombination coefficients. However both 9:1 and 19:1 $CHCl_3$:DCB devices of 0.83 $PC_{70}BM$ composition have a significantly lower recombination coefficient compared to that determined by Eq. (15). This overestimation of the recombination coefficient from Eq. (15) originates from the fact that recombination in the

higher mobility BHJs is no longer diffusion limited as in the Langevin regime but rather becomes kinetic limited as observed in regioregular poly(3-hexylthiophene-2,5-diyl) (P3HT): [6,6]-phenyl C_{61} butyric acid methyl ester (PCBM)[24] and higher mobility inorganic semiconductors. The recombination coefficients derived according to Eq. (14) yield results which are more than an order of magnitude greater than those experimentally determined. The large discrepancies between Eq. (14) and measured recombination coefficients are also observed with P3HT:PCBM.[4]

Figure 4(c) shows the exciton quenching efficiency, η_{ex}, as determined for 9:1 and 19:1 $CHCl_3$:DCB devices for various P(TBT-DPP):$PC_{70}BM$ compositions

$$\eta_{ex} = \eta_{diff}\eta_{diss}. \tag{16}$$

η_{diff} and η_{diss} are exciton diffusion and dissociation efficiency, respectively. Quenching efficiencies are higher in the acceptor domains than the donor domains for both 9:1 and 19:1 $CHCl_3$:DCB devices as a result of the larger electric permittivity of $PC_{70}BM$, increasing η_{diff} by increasing diffusion length.[13] The superior quenching efficiency of 19:1 $CHCl_3$:DCB devices over 9:1 $CHCl_3$:DCB devices is responsible for the difference in short-circuit current (J_{SC}) and higher PCE as seen in Table I. Furthermore, the optimal exciton quenching efficiency occurs at 0.66 and 0.7 $PC_{70}BM$ compositions for 9:1 and 19:1 $CHCl_3$:DCB devices, respectively. The poorer morphology of the 9:1 $CHCl_3$:DCB BHJs not only decreases η_{diff} by virtue of large domain sizes but can also decrease η_{diss} by exacerbating geminate recombination.[25]

The characterized parameters are input in our model to run the device simulations, and the outputs are then compared to the experimental results. To verify the accuracy of the calculated carrier profiles, the measured average total photogenerated carrier concentration extracted from the recombination measurement of a 1:5 P(TBT-DPP):$PC_{70}BM$ 9:1 $CHCl_3$:DCB device is compared to its simulated carrier concentration. Figure 5 compares the measured average photogenerated carrier density, $3 \times 10^{22}\,m^{-3}$, with the modeled electron, hole, and total carrier densities as a function of position in the blend under the same $100\,mW/cm^2$, 532 nm input used in the pump probe technique. The modeled active layer thickness is the same as in the experimental devices with light entering from the anode (right side of Figure 5). The total photogenerated carrier concentration in the center of the active layer (20 nm–110 nm from the cathode) has an average of $2.33 \times 10^{22}\,m^{-3}$ and weighted average of $3.02 \times 10^{22}\,m^{-3}$, which is commensurable with the measured photogenerated carrier density. This similarity confirms the accuracy of the model and characterized parameters of the BHJ.

The accuracy established in the photogenerated carrier profile permits a comparison between the experimental and simulated photogenerated current (J_{ph})–voltage plots. Figure 6(a) shows the experimental and simulated photocurrents using bimolecular recombination coefficients computed from both Eq. (14) and Eq. (15). The poor fit between the experimental and modeled photocurrents using the coefficient

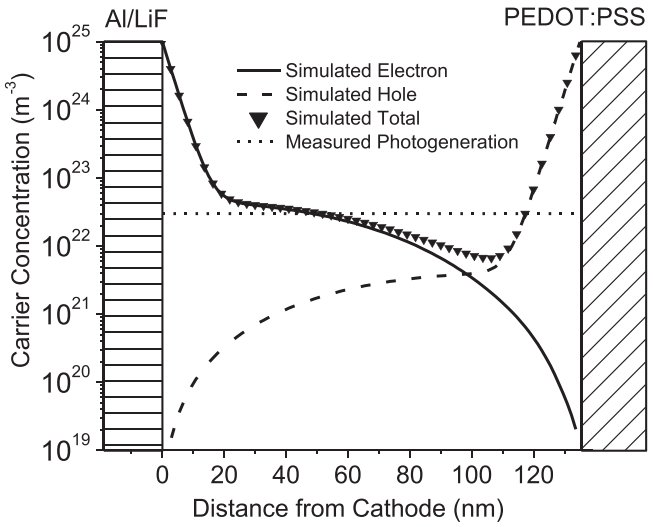

FIG. 5. Comparison between the modeled electron density (solid line), hole density (dashed line), their total density (▼), and the experimentally determined (dotted line) average photogenerated carrier concentration inside a 1:5 P(TBT-DPP):$PC_{70}BM$ composition device cast from 9:1 $CHCl_3$:DCB. The experimental and simulation input conditions are a 532 nm laser of $100\,mW/cm^2$ intensity from the anode (PEDOT:PSS).

obtained by Eq. (14) shows that P(TBT-DPP):$PC_{70}BM$ does not follow homogenous Langevin recombination. Instead Eq. (15), slowest-carrier limited Langevin recombination, yields matching simulated and experimental results. Figure 6(b) shows the comparison between experimental and simulated photocurrents for 3:7 and 1:5 P(TBT-DPP):$PC_{70}BM$ 19:1 $CHCl_3$:DCB devices. Bimolecular recombination coefficients determined both experimentally and from Eq. (15) are input into the model and yield matching results. Not only is the applicability of Eq. (15) valid for all modeled devices but also the fitting between the computed and experimentally determined coefficients for a given device in Figure 6(b) is excellent.

Figure 6(c) shows the spatially varying free-carrier generation rate and non-geminate recombination rate for various applied voltages in the 1:2 P(TBT-DPP):$PC_{70}BM$ 9:1 $CHCl_3$:DCB device modeled using the slowest carrier Langevin recombination coefficient in Figure 6(a). Non-geminate recombination is strongest near the electrodes as a consequence of high carrier densities as mentioned in other modeling accounts.[9] Figure 6(d) also plots generation and recombination but for the 3:7 P(TBT-DPP):$PC_{70}BM$ 19:1 $CHCl_3$:DCB device modeled with the experimentally measured recombination coefficient in Figure 6(b). Generation is maximized in the center of the active region due to optical constructive interference while recombination is dominant near the electrodes as shown in Figures 6(c) and 6(d). As the applied bias increases, the recombination rate intensifies and broadens into the center of the active layer. Recombination rates even exceed generation rates near the electrodes at high voltages for the 9:1 $CHCl_3$:DCB device in Figure 6(c).

DISCUSSION

Experimental and simulation results reveal insights into P(TBT-DPP):$PC_{70}BM$ BHJ OPVs from both a materials

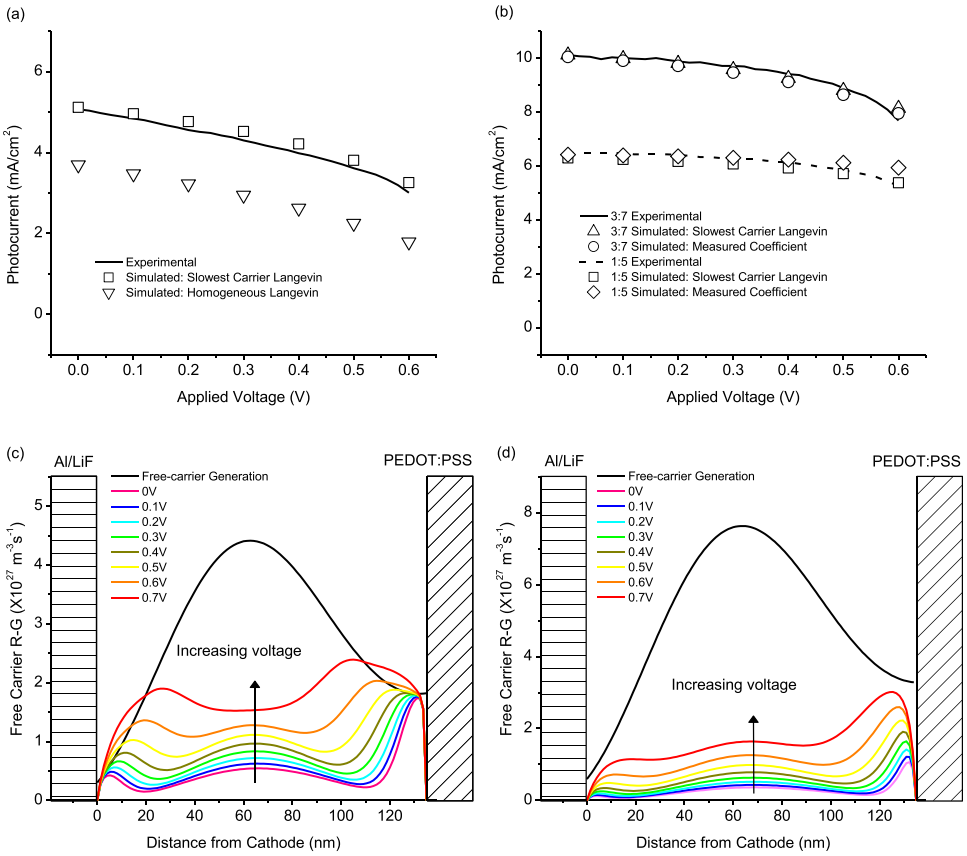

FIG. 6. Modeled photocurrent using homogeneous (Eq. (14)) and slowest-carrier limited Langevin recombination (Eq. (15)) in comparison with the experimental photocurrent for a 1:2 P(TBT-DPP):$PC_{70}BM$ device cast from 9:1 $CHCl_3$:DCB is shown in (a). The modeled photocurrent using slowest-carrier limited Langevin and experimetally determined recombination coefficients for 3:7 and 1:5 P(TBT-DPP):$PC_{70}BM$ devices cast from 19:1 $CHCl_3$:DCB is shown in (b). Generation and non-geminate (free carrier) recombination rates at multiple applied voltages for the device modeled using slowest carrier Langevin recombination from (a) are shown in (c). Generation and non-geminate recombination rates at multiple applied voltages for the 3:7 P(TBT-DPP):$PC_{70}BM$ device modeled using the experimentally determined bimolecular recombination coefficient from (b) are shown in (d).

and devices perspective. Minimization of non-geminate recombination is essential for optimizing the PCE of any photovoltaic device. Carrier mobility plays a crucial role in non-geminate Langevin recombination in that it not only affects the carrier concentration but also determines the bimolecular recombination coefficient as seen from Eqs. (14) and (15). The lack of trap behavior in P(TBT-DPP):$PC_{70}BM$ gives rise to sufficiently high carrier mobilities despite the poor crystalline nature of P(TBT-DPP) and of the corresponding blends (see supplementary material for XRD results[34]). Contrarily, high performance amorphous polymer poly[[9-(1-octylnonyl)-9H-carbazole-2,7-diyl]-2,5-thiophenediyl-2,1,3-benzothiadiazole-4,7-diyl-2,5-thiophenediyl] (PCDTBT):$PC_{70}BM$ BHJs show a significant decrease in fill factor for thicknesses greater than only 70 nm as a result of non-geminate recombination due to hole trapping.[26]

Further insights are made into the nature of non-geminate recombination in our BHJs by modeling the photocurrent. Koster *et al*. observed that non-geminate recombination in P3HT:PCBM is limited by the slowest carriers by comparing the fill factor amongst various recombination models.[23] In addition to the similarity between experimental and computed (Eq. (15)) bimolecular recombination coefficients, matching experimental and simulated photocurrents modeled using both measured and computed bimolecular recombination coefficients (Figure 6(b)) provides strong evidence that the lowest carrier mobility in a BHJ indeed limits non-geminate recombination. With these findings for P3HT, as well as for poly[2-methoxy-5-(2-ethylhexyloxy)-1,4-phenylenevinylene] (MEH-PPV)[23] and P(TBT-DPP), it is believed that Eq. (15) can be used to model bimolecular recombination in a wide range of photoactive materials for BHJ OPVs.

The close match between modeled and experimental photocurrents for all the modeled devices validates our model and BHJ characterization, allowing us to faithfully examine the non-geminate recombination rates inside our devices. Low mobility, high free-carrier generation rates, and low electric fields exacerbate non-geminate recombination by virtue of high carrier densities. It is for these reasons non-geminate recombination rates reach a local maximum in the center of the device, where optical interference maximizes generation rate, and then even higher rates at the electrodes where carrier concentrations build up to even higher densities as seen in Figures 6(c) and 6(d). In comparison to the 9:1 $CHCl_3$:DCB device in Figure 6(c), the reduction in non-geminate recombination rate relative to generation rate at the electrodes of the 19:1 $CHCl_3$:DCB device in Figure 6(d) is not only a consequence of higher BHJ mobility and lower bimolecular recombination but also decreased electron and hole carrier concentrations at the cathode and anode, respectively. For this reason, decreasing this electrode carrier concentration by decreasing the density of states can reduce recombination in the vicinity of the electrodes. Another route for reducing recombination may be to morphologically grade the electrode regions to increase carrier mobility at the expense of generation. Indeed, high performance BHJ OPVs do show significant improvement when the donor–acceptor composition near the electrodes yield higher mobilities.[27,28] Our model is capable of taking into account varying donor–-acceptor compositions as a function of depth which can be used for future device optimization.

The comparisons between the experimental data and modeled data demonstrate that it is possible to accurately describe the device physics of OPVs without fitting parameters. Furthermore, physical quantities that are experimentally inaccessible (or challenging to access) such as non-radiative dissociation rates and electron-hole separation distances at interfaces[9,23] are avoided in our model. Exciton dissociation efficiency, η_{diss}, was believed to be field-dependent according to Braun-Onsager theory,[8,29] but experiments by Mauer and Etzold *et al*. have shown that the dissociation behavior for polythiophene-methanofullerene and PCDTBT-$PC_{70}BM$ composites is in fact field-independent.[3,26] This behavior stems from the high conjugation length of high performance OPV BHJs.[30] Consequently, the measured η_{diss} is taken to be the same for any applied bias in the model.

Despite the accurate results demonstrated here for low and high performance devices made from P(TBT-DPP):$PC_{70}BM$, not all material systems can be accurately modeled using the approximations made in this work. For low-mobility BHJ blends where carrier concentrations are expected to be high, the Einstein relationship dependence on carrier concentration should be evaluated.[15] In extreme cases, space-charge may need to be taken into account in device with low-mobility BHJs and thick exciton blocking layers.[31] The appropriate SCLC fitting curve should be chosen in order to ascertain mobility, since high trap densities affect the SCLC dependence on the applied voltage and the active layer thickness.[32] Experimentally determining the input parameters associated with a particular morphology in a morphologically graded as-cast device can be achieved by making sufficiently thick films to decrease the influence of near surface regions on the active layer. Finite surface recombination velocity may also be taken into account and are derivable for organic-metal interfaces using a detailed balance limit.[33] Finally, the absorption spectra for P(TBT-DPP):$PC_{70}BM$ BHJs show some differences compared to the superposition of P(TBT-DPP) and $PC_{70}BM$ most likely as a result of some expected P(TBT-DPP)-$PC_{70}BM$ phase formation, meaning that there are limits to the accuracy with which absorption can be modeled as a superposition of donor and acceptor absorptions.

There are also limitations in the model itself. The V_{oc} for the tested devices is approximately 0.7 V as shown in Table I, but the photocurrent is only modeled until 0.6 V since the injection current induces significant recombination with the photocurrent approaching V_{oc}, making it impractical to solely consider photogeneration current for device modeling in this region. The measured exciton quenching efficiencies exhibited the greatest error range of all the material parameters measured as the result of sensitivity to sample positioning. Finally, in the class of material systems with poor conjugation length where exciton-quenching is field dependent[30] (which would have very poor fill factors) a coupling between the charge generation rate and the field would need to be introduced which we neglect in the current treatment. However, despite these limitations, we strongly believe that our model is a valuable and easily applicable tool that is widely useful for understanding of the processes occurring in OPV devices. We hope it will find use in aiding targeted device optimization within the OPV community.

CONCLUSIONS

Developing upon previous device models, we present a computationally non-intensive model based entirely on experimentally available empirical parameters. The model parameters are experimentally determined using common-place techniques, and, without any fitting parameters, our model accurately reproduces the experimental photocurrent curves for a wide variety of device processing conditions. We compare two experimental methods for determining the bimolecular recombination coefficient and find that both work well, reproducing accurately the measured photocurrent curve. From this we conclude that slowest-carrier limited Langevin recombination accurately describes recombination in our devices and therefore may be a good starting point for determination of the bimolecular recombination coefficient in general. With the accuracy of the model established, it can be used to provide insight into the generation, non-geminate recombination, hole and electron concentrations as a function of depth within the operating cell. These results (which are not experimentally observable) can then be utilized to pinpoint the weaknesses and strengths of the devices. This can be a general aid in targeted device engineering. Morphologically graded BHJ OPVs can be engineered to improve upon the power conversion efficiency by maximizing generation in the center of the active layer while minimizing recombination near the electrodes. We hope that the speed, simplicity, and accuracy of the present model will make it generally useful to the broad community investigating organic bulk heterojunction solar cells (see supplementary material for the simulation program used in this publication).[34]

ACKNOWLEDGMENTS

This work was partially supported by the National Science Foundation under Grant No. ECCS-1202189 and under the National Science Foundation Graduate Fellowship Research Program under Grant No. DGE-1106400. Portions of this work were performed as user project #1289 at the Molecular Foundry, supported by the Office of Science, Office of Basic Energy Sciences, of the U.S. Department of Energy under Contract No. DE-AC02-05CH11231. The authors would like to thank Teresa Chen and Biwu Ma in The Molecular Foundry at Lawrence Berkeley National Laboratory for training and access to device fabrication and characterization equipment, and Rachel Segalman for access to fabrication equipment.

[1]S. Rohr, Heliatek (2012), see http://www.heliatek.com/wp-content/uploads/2013/01/130116_PR_Heliatek_achieves_record_cell_effiency_for_OPV.pdf for information about this company.
[2]Alexandra K. Duncan, Materials360 Online (2012), see http://www.materials360online.com/newsDetails/13040 for more information about this company.
[3]R. Mauer, I. A. Howard, and F. Laquai, J. Phys. Chem. Lett. **1**(24), 3500 (2010).
[4]R. Mauer, I. A. Howard, and F. Laquai, J. Phys. Chem. Lett. **2**(14), 1736 (2011).

[5]G. A. H. Wetzelaer, L. J. A. Koster, and P. W. M. Blom, Phys. Rev. Lett. **107**(6), 066605 (2011).
[6]W. F. Pasveer, J. Cottaar, C. Tanase, R. Coehoorn, P. A. Bobbert, P. W. M. Blom, D. M. de Leeuw, and M. A. J. Michels, Phys. Rev. Lett. **94**(20), 206601 (2005).
[7]Sentaurus Device (Synopsys, 2011), see http://www.synopsys.com/Tools/TCAD/DeviceSimulation/Pages/SentaurusDevice.aspx for more information about this company.
[8]P. W. M. Blom, V. D. Mihailetchi, L. J. A. Koster, and D. E. Markov, Adv. Mater. **19**(12), 1551 (2007).
[9]L. J. A. Koster, E. C. P. Smits, V. D. Mihailetchi, and P. W. M. Blom, Phys. Rev. B **72**(8), 085205 (2005).
[10]J. D. Kotlarski, P. W. M. Blom, L. J. A. Koster, M. Lenes, and L. H. Slooff, J. Appl. Phys. **103**(8), 084502 (2008).
[11]G. F. Burkhard, E. T. Hoke, and M. D. McGehee, Adv. Mater. **22**(30), 3293 (2010).
[12]M. M. Mandoc, L. J. A. Koster, and P. W. M. Blom, Appl. Phys. Lett. **90**(13), 133504 (2007).
[13]B. A. Gregg and M. C. Hanna, J. Appl. Phys. **93**(6), 3605 (2003).
[14]A. Petersen, T. Kirchartz, and T. A. Wagner, Phys. Rev. B **85**(4), 045208 (2012).
[15]Y. Roichman and N. Tessler, Appl. Phys. Lett. **80**(11), 1948 (2002).
[16]S. Günes, H. Neugebauer, and N. S. Sariciftci, Chem. Rev. **107**(4), 1324 (2007).
[17]T. Kirchartz, B. E. Pieters, K. Taretto, and U. Rau, J. Appl. Phys. **104**(9), 094513 (2008).
[18]A. J. Moule and K. Meerholz, Adv. Funct. Mater. **19**(19), 3028 (2009).
[19]S. Yamamoto, J. Guo, H. Ohkita, and S. Ito, Adv. Funct. Mater. **18**(17), 2555 (2008).
[20]R. Pandey and R. J. Holmes, Adv. Mater. **22**(46), 5301 (2010).
[21]C. Deibel, T. Strobel, and V. Dyakonov, Adv. Mater. **22**(37), 4097 (2010).
[22]A. Pivrikas, H. Neugebauer, and N. S. Sariciftci, IEEE J. Sel. Top. Quantum Electron. **16**(6), 1746 (2010).
[23]L. J. A. Koster, V. D. Mihailetchi, and P. W. M. Blom, Appl. Phys. Lett. **88**(5), 052104 (2006).
[24]A. Pivrikas, N. S. Sariciftci, G. Juska, and R. Osterbacka, Prog. Photovoltaics **15**(8), 677 (2007).
[25]F. Etzold, I. A. Howard, N. Forler, D. M. Cho, M. Meister, H. Mangold, J. Shu, M. R. Hansen, K. Mullen, and F. Laquai, J. Am. Chem. Soc. **134**(25), 10569 (2012).
[26]F. Etzold, I. A. Howard, R. Mauer, M. Meister, T. D. Kim, K. S. Lee, N. S. Baek, and F. Laquai, J. Am. Chem. Soc. **133**(24), 9469 (2011).
[27]L. M. Chen, Z. R. Hong, G. Li, and Y. Yang, Adv. Mater. **21**(14-15), 1434 (2009).
[28]C. M. B. Svanstrom, J. Rysz, A. Bernasik, A. Budkowski, F. Zhang, O. Inganas, M. R. Andersson, K. O. Magnusson, J. J. Benson-Smith, J. Nelson, and E. Moons, Adv. Mater. **21**(43), 4398 (2009).
[29]T. Kirchartz, K. Taretto, and U. Rau, J. Phys. Chem. C **113**(41), 17958 (2009).
[30]C. Schwarz, H. Bassler, I. Bauer, J. M. Koenen, E. Preis, U. Scherf, and A. Kohler, Adv. Mater. **24**(7), 922 (2012).
[31]J. C. Wang, X. C. Ren, S. Q. Shi, C. W. Leung, and P. K. L. Chan, Org. Electron. **12**(6), 880 (2011).
[32]Z. M. Beiley, E. T. Hoke, R. Noriega, J. Dacuna, G. F. Burkhard, J. A. Bartelt, A. Salleo, M. F. Toney, and M. D. McGehee, Adv. Energy Mater. **1**(5), 954 (2011).
[33]J. C. Scott and G. G. Malliaras, Chem. Phys. Lett. **299**(2), 115 (1999).
[34]See supplementary material at http://dx.doi.org/10.1063/1.4801662 for TEM tomography images, XRD images, and optical constants. The MATLAB program of our model is open source and available at http://www.mathworks.com/matlabcentral/fileexchange/ under the file name "Bulk Heterojunction Device Model" or from the Ana Claudia Arias research group homepage.